Int. J. Heat Mass Transfer. Vol. 36, No. 5, pp. 1391–1401, 1993
Printed in Great Britain

0017–9310/93 $6.00 + 0.00

Analysis and numerical simulation of the thermohydraulic behaviour of a heat dissipating debris bed during power transients

A. K. STUBOS and J.-M. BUCHLIN
von Karman Institute for Fluid Dynamics, Rhode-Saint-Genèse, Belgium

(*Received* 17 *September* 1990 *and in final form* 5 *January* 1991)

Abstract—A mathematical model for the description of the transient behaviour of a liquid saturated core debris bed with internal heat dissipation is formulated and solved numerically. The development is supported by the findings of an out-of-pile investigation of the relevant phenomenology. Furthermore the data from the Sandia Laboratories D10 in-pile test as well as from the first European in-pile experiment designed to study, in the frame of the Post Accident Heat Removal Programme, the long term coolability of such a bed, are used for the validation of the model.

1. INTRODUCTION

THE PRESENT paper deals with a multi-dimensional model describing the transient thermohydraulic behaviour of a liquid saturated, self heated fine-debris bed, the formation of which is postulated after severe accident sequences in Liquid Metal Fast Breeder nuclear Reactors (LMFBR) in the frame of the Post Accident Heat Removal Scenario (PAHR) [1]. The heat generated in the bed may be removed by conduction, natural convection and phase change processes. The onset and evolution of a dry zone in the boiling region of the bed mark a sharp change in the coolability of the system and consequently their prediction is of special interest in this safety analysis problem. In addition, out-of-pile and in-pile experimental findings indicate that the occurrence of bed disturbances, either natural or due to fast power transients, affects significantly the power levels needed to provoke dryout conditions. Therefore the necessity of unsteady computational simulations for the analysis of the problem and the interpretation of test results becomes apparent. After discussing the physical model on which the present approach relies, the mathematical formulation and the main features of the numerical method are presented. The applicability of the model is exemplified through comparisons of the numerical predictions with the results of the VKI out-of-pile tests [2], and the in-pile data obtained during the European PIRAMID-1 [3] and the Sandia Laboratories D10 [4] experiments.

2. THE PHYSICAL MODEL

The complex thermohydraulic behaviour of the debris bed is sketched in Fig. 1. The different characteristic regions and the associated heat transfer modes are identified. For the sake of generality top- and bottom-cooled beds are considered.

- As the top surface of the bed is maintained at a constant temperature by the overlying liquid coolant layer, the first upper zone is subcooled. Heat transfer by conduction and single phase natural or forced convection may take place.
- The top boiling zone forms as saturation conditions are reached. It is assumed isothermal and characterized by counter- or co-current two phase flow.
- Dryout occurs when the downcoming liquid cannot replenish the porous matrix due to high vapour production, and the liquid fraction, s (also called saturation), drops locally to zero. Conduction, convection and radiation contribute to heat transfer from the dry zone but the poor thermal conductivity of the vapour leads to rather high temperature gradients in this region.

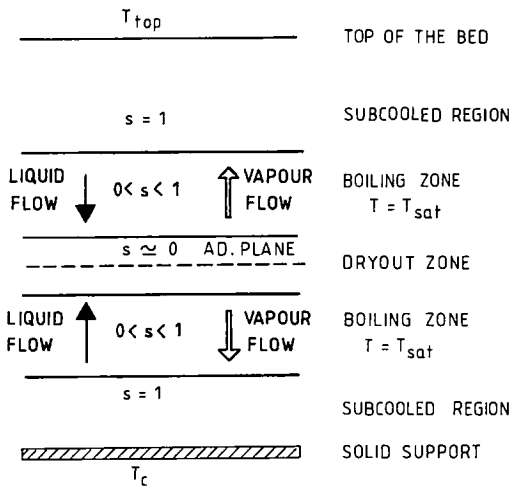

FIG. 1. Thermohydraulic zones in the debris bed.

NOMENCLATURE

A_1, A_2, A_4, A_5 non-dimensional parameters
Bi non-dimensional heat transfer coefficient, hH/λ
C_p specific heat [J kg^{-1} K^{-1}]
g gravitational acceleration [m s^{-2}]
h heat transfer coefficient [W m^{-2} K^{-1}]
H height of the bed [m]
h_{lv} latent heat [J kg^{-1}]
J Leverett function
P pressure [Pa]
Q volumetric power [W m^{-3}]
T temperature [K]
t time [s]
Δt time step [s]
V superficial velocity [m s^{-1}]
z vertical coordinate [m].

Greek symbols
γ kinematic viscosity ratio, ν_l/ν_v
ε porosity
η specific heat ratio, C_{pv}/C_{pl}
θ contact angle
κ permeability [m^2]
κ_l, κ_v relative permeabilities
λ effective conductivity [W m^{-1} K^{-1}]
μ dynamic viscosity [kg m^{-1} s^{-1}]
ν kinematic viscosity [m^2 s^{-1}]
ρ density [kg m^{-3}]
σ surface tension [N m^{-1}]
ϕ density ratio, ρ_l/ρ_v.

Subscripts
b boiling
c cooling or capillary
f fluid
l liquid
n numerical
s solid
t at time level t
top at the bed top
v vapour.

Superscript
* non-dimensional quantity.

Non-dimensional variables and constants
A_1 $\lambda T_b/QH^2$
A_2 $(\sigma\sqrt{(\varepsilon/\kappa)})/(\nu_v H^2 Q/\kappa h_{lv})$
A_4 $\varepsilon\rho_v h_{lv}/((\rho_s C_{ps}(1-\varepsilon)+\rho_l C_{pl}\varepsilon)T_b)$
A_5 $C_{pl}T_b/h_{lv}$
λ^* $\lambda/\lambda_{subcooled}$
P^* $P\kappa h_{lv}/\nu_v H^2 Q$
T^* $(T-T_b)/T_b$
$(\rho g)^*$ $\rho g H/(\nu_v H^2 Q/\kappa h_{lv})$
$(\rho V)^*$ $\rho V h_{lv}/HQ$
t^* $[t/(\rho_s C_{ps}(1-\varepsilon)+(\rho_l C_{pl}\varepsilon)T_b)]/Q$.

• Bottom cooling divides the bed through an adiabatic plane located inside it and induces the formation of a bottom subcooled zone separated from the dry region by a second boiling regime. Due to the small size of the particles (100–1000 μm) capillarity overcomes buoyancy and downward boiling occurs.

3. THE MATHEMATICAL FORMULATION AND THE NUMERICAL SOLVER

A multi-dimensional mathematical model is developed on the basis of the above physical approach assuming thermal equilibrium between the solid and fluid phases (thermally homogeneous medium [5]).

Darcy's law is applied as the equation of motion in the single phase zones (dry and subcooled) of the bed while incompressibility provides the form of the mass balance

$$\nabla P + \frac{\nu}{\kappa}\rho\mathbf{V} + \rho\mathbf{g} = 0 \tag{1}$$

$$\nabla\mathbf{V} = 0. \tag{2}$$

An effective conductivity coefficient, depending on the physical properties of the solid and fluid phases and the temperature, is used to account for mechanisms such as free convection (upper subcooled region) or radiation (dry area)

$$(\rho C_p)_{bed}\frac{\partial T}{\partial t} + (\rho C_p)_f \mathbf{V}\nabla T - \nabla(\lambda\nabla T) = Q \tag{3}$$

where the bed heat capacity is defined as

$$(\rho C_p)_{bed} = (1-\varepsilon)\rho_s C_{ps} + \varepsilon\rho_f C_{pf}.$$

For the two-phase flow regime the phasic Darcy's law based on the local relative permeability function of saturation is applied [5]

$$\nabla P_i + \frac{\nu_i}{\kappa\kappa_i}\rho_i\mathbf{V}_i + \rho_i\mathbf{g} = 0 \tag{4}$$

with i = l, v and

$$\kappa_l = s^3, \quad \kappa_v = (1-s)^2.$$

The important driving effect of capillarity, expressed as a pressure differential between the vapour and liquid phases, is included through the use of the Leverett function of the liquid fraction

$$P_c = P_v - P_l = \sigma\cos\theta\sqrt{\left(\frac{\varepsilon}{\kappa}\right)}J(s) \tag{5}$$

where

$$J(s) = \frac{(1-s^{-1})^{0.175}}{\sqrt{5}}.$$

The mass and energy balances in the boiling part of the debris bed, the latter simply describing the phase change process, complete the set of equations for the transient thermohydraulic behaviour of a heat dissipating particulate bed

$$\varepsilon(\rho_l-\rho_v)\frac{\partial s}{\partial t}+\nabla(\rho_l\mathbf{V}_l+\rho_v\mathbf{V}_v)=0 \quad (6)$$

$$-\varepsilon\rho_v h_{lv}\frac{\partial s}{\partial t}+h_{lv}\nabla(\rho_v\mathbf{V}_v)=Q. \quad (7)$$

An 'enthalpic' approach is adopted in order to avoid tracking of the interfaces between the different bed zones and to relax the numerical difficulties posed by the discontinuous temperature gradients at these interfaces as a result of the thermal equilibrium assumption. It consists of relating temperature and liquid fraction through a suitable smoothing function after observing that when one variable changes the other remains constant and vice versa (see Fig. 2). The Kelvin and Clapeyron equations provide the physical ground for such a relationship. Their combination yields the temperature as a function of the capillary pressure, i.e. saturation according to equation (5) [6]. The different mass, momentum and energy equations can then be merged in a single set valid throughout the bed, keeping in mind the eventual variation of the effective conductivity coefficient and the heat capacities in the subcooled and dry regions. In this way the two-phase region becomes 'nearly' isothermal in the sense that the boiling temperature varies slightly within it. Additionally vapour pressure lowering effects are taken into account although their importance is minor for the present range of bed permeabilities [7].

Casting of the governing equations produces after non-dimensionalization a system of two coupled highly nonlinear partial differential equations to be solved for the temperature T^* and liquid pressure P_l^* in the bed

$$(\rho C_p)^*\frac{\partial T^*}{\partial t^*}-A_4\frac{\partial s}{\partial t^*}-\nabla\{\kappa_v\nabla(P_l^*+A_2J)\}$$
$$-A_1\nabla(\lambda^*\nabla T^*)-A_5\left\{\frac{\kappa_l}{\gamma}(\nabla P_l^*+(\rho_l g)^*)\right.$$
$$\left.+\eta\kappa_v\nabla(P_l^*+A_2J)\right\}\nabla T^*=Q^* \quad (8)$$

$$A_4(\varphi-1)\frac{\partial s}{\partial t^*}-\nabla\left\{\frac{\kappa_l}{\gamma}(\nabla P_l^*+(\rho_l g)^*)\right.$$
$$\left.+\kappa_v\nabla(P_l^*+A_2J)\right\}=0. \quad (9)$$

The computational domain consists of a rectangle with the axis of symmetry forming one of its sides. The boundary conditions are specified as follows:

top: imposed T^*_{top} and $P^*_{l,top}$;

bottom: impermeable wall and heat losses through a finite heat transfer coefficient Bi and a given external cooling temperature T_c^*

$$\{-A_1\lambda^*\nabla T^*-\kappa_v\nabla P_v^*\}\mathbf{n}=A_1\,Bi(T_c^*-T^*); \quad (10)$$

left: axisymmetry;

right: similar to the bottom one.

Using successive substitution of the two unknowns the equations can be solved separately and the numerical problem one is faced with becomes how to solve a nonlinear unsteady Poisson equation throughout the bed, i.e.

$$\frac{\partial T^*}{\partial t^*}+\text{sp.op}(T^*)=0 \quad (11)$$

with T^* the unknown and sp.op denoting the space operators which include the diffusive, convective and source terms. Employing the trapezoidal formula for a second-order accurate time discretization yields

$$\frac{T^*_{i^*+1}-T^*_{i^*}}{\Delta t_p^*}+\tfrac{1}{2}\{\text{sp.op}(T^*_{i^*+1})+\text{sp.op}(T^*_{i^*})\}=0 \quad (12)$$

and introducing a numerical time derivative that allows the application of a fast converging, non-accurate, time-marching technique gives

$$\frac{T_n^*-T_{n-1}^*}{\Delta t_n^*}+\frac{T_n^*-T^*_{i^*}}{\Delta t_p^*}$$
$$+\tfrac{1}{2}\{\text{sp.op}(T_n^*)+\text{sp.op}(T^*_{i^*})\}=0 \quad (13)$$

where Δt_p^* and Δt_n^* represent the physical and numerical time-steps, respectively.

As the method converges

$$\lim_{n\to\infty}\frac{T_n^*-T_{n-1}^*}{\Delta t_n^*}=0$$

and consequently T_n^* tends to $T^*_{i^*+1}$, i.e. the solution at the new physical time level. The implicit approximate

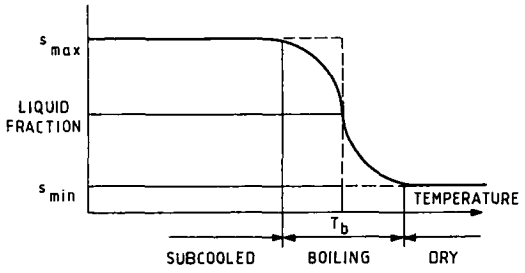

FIG. 2. The s–T enthalpic function.

factorization scheme based on the 'δ' formulation of the main variables is chosen as such a controllable iterative procedure for the solution in two dimensions of the centrally discretized form of the equations on a uniform rectangular grid [8]. The axisymmetric boundary condition is implemented implicitly while the others are treated explicitly in the code. An analytical estimation of the optimal numerical time-step is incorporated to minimize the computational effort for the transient calculations in the present diffusion dominated nonlinear case [9]. In this sense the physical time-step is limited only by the desirable resolution of the unsteadiness of the physical problem.

4. APPLICABILITY OF THE MODEL

A major experimental study of the PAHR situation in a LMFBR environment is currently underway at the nuclear centre of Mol, Belgium. The first of the four planned in-pile tests, named PIRAMID-1, was successfully executed in November 1986. The test section consists of the crucible (internal diameter of 0.11 m) containing the debris bed and the sodium pool above it, with a possible range for the pressure of the argon cover gas between 1 and 5 bar [3]. The debris bed is formed by 10 kg of UO_2 particles immersed in liquid sodium and heated by the neutrons and gamma irradiation of the reactor. Initially it is characterized by a height of 0.146 m, an effective particle diameter of 230 μm and a porosity of 32%. It is cooled from the top and bottom via suitable heat exchanger circuits and undergoes heat losses in the radial direction. The power deposition in the bed is not uniform; it exhibits a radial variation with a maximum at the wall. Temperatures are measured mainly by high-temperature thermocouples distributed in the porous matrix as indicated in Fig. 3. Additional information on the Na vapour production is provided by a Na level indicator at the top of the liquid sodium pool overlying the bed.

A series of steady state 2D calculations based on the aforementioned model have already shown its consistency in predicting typical cases referring to the main stages of the experimental procedure followed during the PIRAMID-1 test, as discussed in detail in ref. [10]. They include the bed calibration procedure, aiming mainly at the determination of the effective thermal conductivity coefficient under subcooled bed conditions, the incipient boiling of the liquid sodium and the onset of dryout under varying cooling conditions and system pressure. Presently the interest is focused on the simulation and interpretation of some important effects of transient nature observed during the test.

Three power ramps were performed in order to provoke sudden vapour production in the bed and subsequently disturb the upper part of it. This type of disturbance should be distinguished from the ones caused by liquid sodium superheating which is not

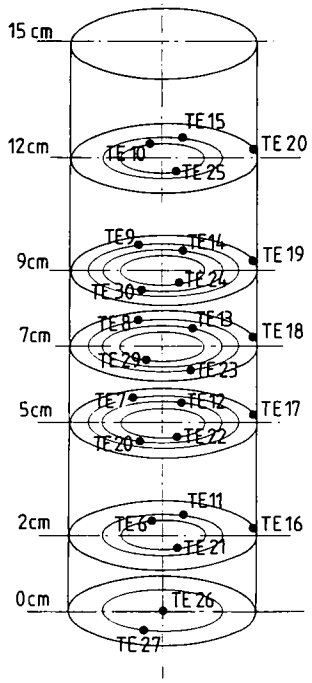

FIG. 3. Thermocouple locations in the PIRAMID-1 bed.

observed during the presently studied power surges for the simple reason that the ramp initially starts from a boiling situation. Nevertheless the outcome of superheat flashing in the bed is thought to be similar to that of steep power increases with the important difference that the initial experimental conditions are far more precisely known and controlled in the latter case. The objective is to simulate the initial stages of a real accident case when the particles are still highly radioactive and to study the effect of possible bed disruptions on its coolability, since previous in- and out-of-pile tests have provided evidence for a possible enhancement of the power deposition needed to induce dryout [11]. Such steep power increases are necessary since the 'natural' occurrence of bed structural changes like vapour channel formation, as observed during out-of-pile tests [12], is prohibited here by the thick top subcooled zone. Indeed the conductivity of the PIRAMID-1 bed is found equal to 23 $W m^{-1} K^{-1}$ in ref. [10] as opposed to a value of about 3 $W m^{-1} K^{-1}$ characterizing the bed of dielectrically heated ferrite particles (320 μm effective diameter) in water, used in the out-of-pile facility set up at VKI and code named OPERA [2, 12].

The phenomenology of the disturbances has been studied for the first time out-of-pile and the results obtained are described next along with the corresponding numerical computations. The insight thus gained proves of great help for the interpretation of the visually inaccessible PIRAMID-1 and D10 in-pile tests.

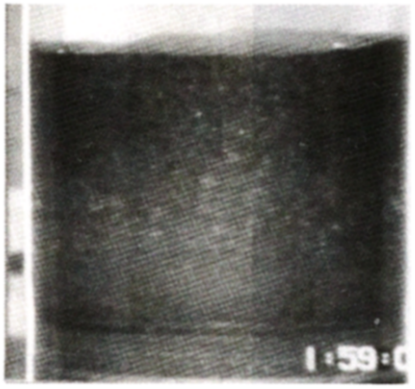

(a) Packed state

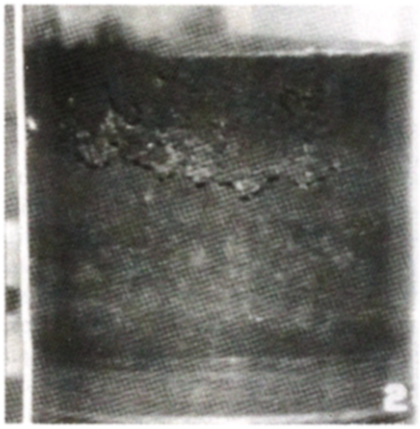

(b) Crack formation

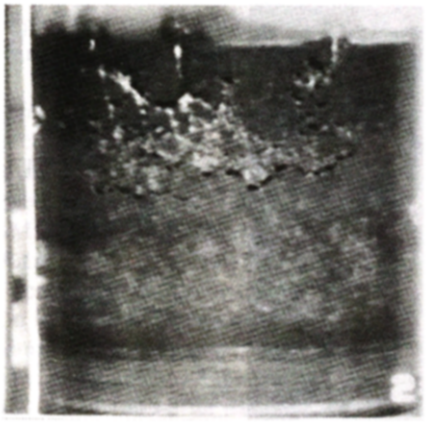

(c) Channel penetration

FIG. 4. Provoked channel formation: (a) packed state; (b) crack formation; (c) channel penetration.

Out-of-pile investigation

The sequence of photographs presented in Fig. 4 is a typical visualization of the occurrence of disturbances after a sharp power ramp in a 0.1 m deep OPERA bed. It reveals the relevant mechanism as the initially packed bed (Fig. 4(a)) is separated in two regions by a deep crack due to the sudden high vapour generation (Fig. 4(b)).

In fact the induced rate of vapour production causes, locally, a fast increase in vapour pressure with time, while the restriction of the cross-section available for the upward vapour flux, because of the presence of the liquid, is such that a steep vapour pressure gradient develops. The disturbance is likely to occur somewhere above the position of the adiabatic plane before the application of the ramp and preferably just behind the moving vapour front, where the gradients are sharper, as soon as the vapour pressure is high enough to lift the overlying bed [13]. This is clearly depicted in Fig. 5 where the transient calculation for the present case predicts the occurrence of the disturbance (Fig. 4(b)) 10 s after the ramp, at a level of 7.5 cm from the bed bottom in accordance with the experiment. A computed average expansion of 0.29 mm s^{-1} for the top liquid level as compared to an experimental value of 0.3 mm s^{-1} further stresses the agreement.

A few seconds later the accumulated vapour penetrates to the bed top forming stable or unstable channels (Fig. 4(c)). A requirement for this final stage of the process is that the vapour front moves upward during the transient with a speed high enough to cause its destabilization in a finger-like manner [14] and the opening of channels. Furthermore the formation of the crack should not result in a relief of pressure. In such a case the crack would tend to close and re-open setting the upper part of the bed in a continuous heaving motion. This type of behaviour is actually observed as the power is increased in small steps during a quasi-steady approach to dryout in the bed. The top part stops vibrating and comes to rest only after the formation of the dry zone which, as a single phase regime, relaxes the vapour pressure. Eventually the pressure behind the crack continues to build up only when the rate of vapour production exceeds the upward acceleration of the slug

$$\frac{\partial V_v}{\partial t} > \frac{P_v}{L_{dis}[(1-\varepsilon)\rho_s + \varepsilon\rho_l]} - g \qquad (14)$$

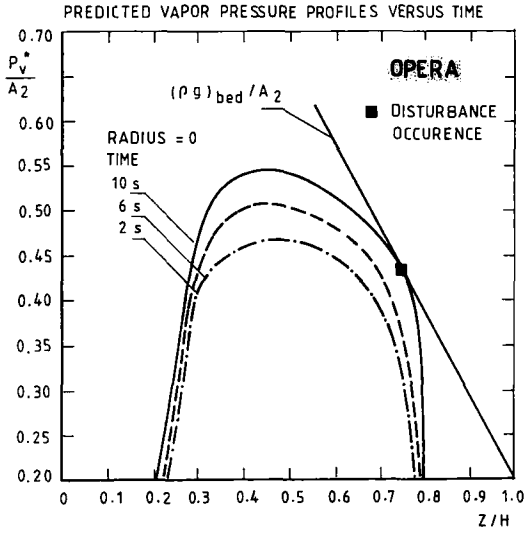

FIG. 5. Computed profiles of vapour pressure during power ramp in OPERA bed.

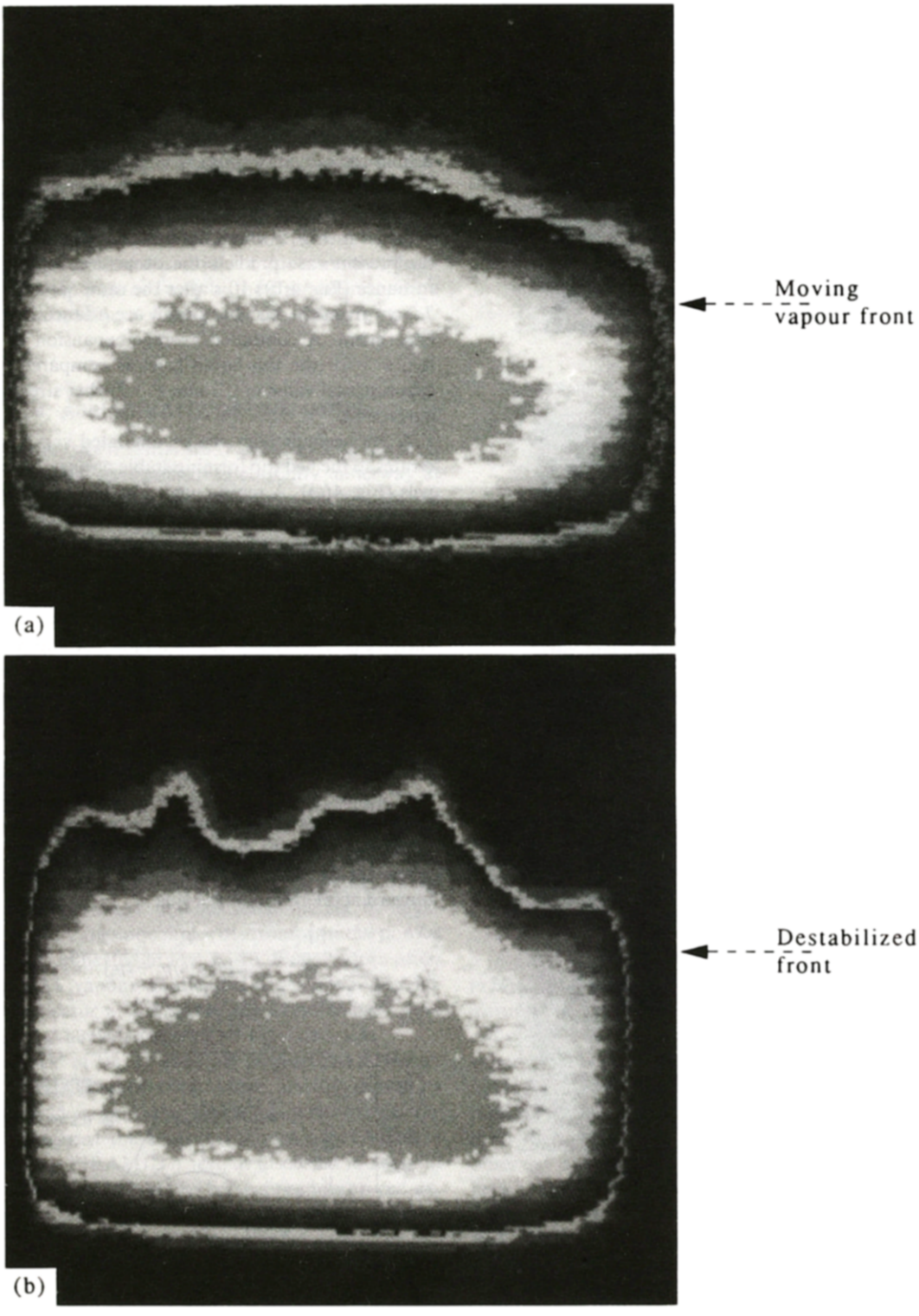

FIG. 6. Digitized infrared images of the vapour front propagation in OPERA bed: (a) before disturbance; (b) occurrence of disturbance.

i.e. if the power ramp is strong enough and the initial bed conditions such that P_v is moderate (e.g. small initial boiling region). Here L_{dis} denotes the length of the disturbed bed regime.

The vapour front propagation has also been filmed with an infrared camera, and Fig. 6 displays the false-colour thermograms corresponding to the time instant just before and just after the onset of the disturbance (formation of the crack). It can be deduced that, as the vapour slug displaces the overlying bed up-

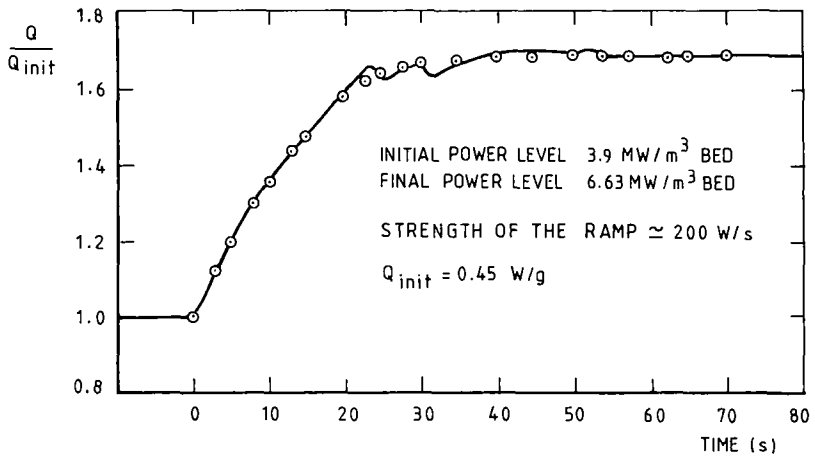

FIG. 7. PIRAMID-1 in-pile experiment: the second power ramp (PR2).

ward (unstable configuration), the occurring Taylor instability manifests itself via the wavelength pattern appearing in Fig. 6. A physical model for the channel population density can be proposed on the basis of the presently revealed mechanism. In fact one may well expect that in this case the Taylor cutoff wavelength, given by linear stability theory, predicts accurately enough the observed channel pattern [5]. The reason is that the initial amplified perturbation at the vapour/bed interface results in the expulsion of particles and the opening of channels, thus freezing the original pattern before non-linearities become dominant.

Simulation and interpretation of in-pile experiments

The conclusions reached with the aid of the out-of-pile tests and the 2D transient computations are employed presently for the interpretation of the PIRAMID-1 and D10 experiments.

PIRAMID-1 test. A total of three power ramps were performed to provoke sudden vapour production in the bed. The second one (PR2, see Fig. 7) caused a disturbance easily identified by the readings of the thermocouples and the Na level indicator (Figs. 8 and 9) about 100 s after its execution. As indicated in these figures, at 80 s both the Na level and thermocouple TE10 (located 12 cm from the bed bottom and 24 mm in radius, see Fig. 3) start deviating from the computed values. This moment corresponds to the situation shown in Fig. 4(b). Indeed the slight lifting of the upper part brings TE10 at a deeper and consequently hotter location in the bed and that is expressed by temperature readings higher than the predicted (Fig. 8). TE26 as well as TE21 obviously lie below the disturbance location and therefore remain unaffected by it. On the other hand the formation of the cracks and cavities offers space for the accumulation and compression of the vapour thus retarding the increase of the top liquid level and explaining the overprediction in Fig. 9. This last liquid level evolution is based on the computed liquid mass flux out of the bed top as a result of the boiling zone expansion (Fig. 10). Some 20 s later the vapour breaks through the top part and its passage is recorded as a spike by both TE10 and the Na level indicator. This is equivalent to the behaviour displayed in Fig. 4(c).

After predicting the time of occurrence, the next step is to determine where the disturbance arises. The adiabatic plane location, before the ramp, is predicted to be at 6.3 cm from the bottom. Figure 11 shows the

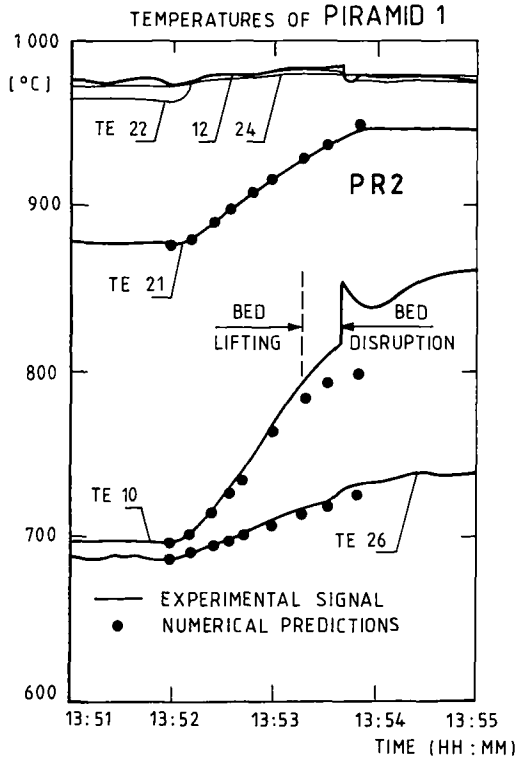

FIG. 8. Experimental and predicted thermocouple histories during PR2.

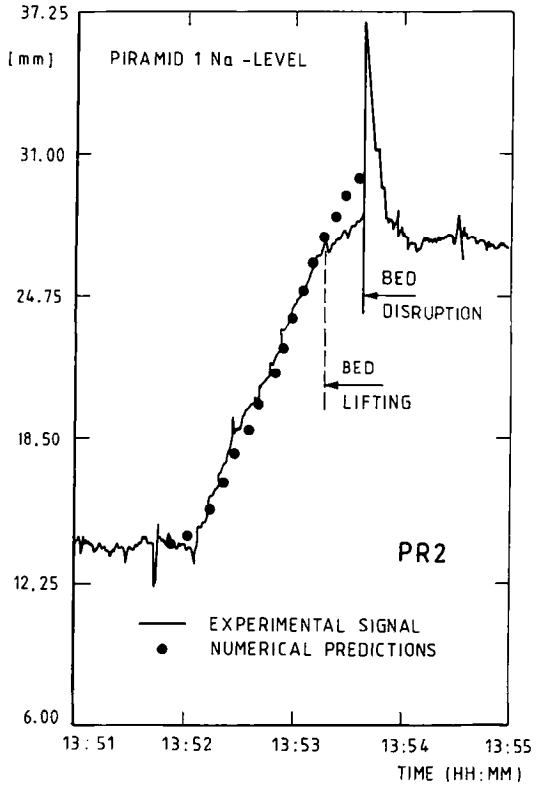

FIG. 9. Experimental and predicted Na level expansion during PR2.

computed profiles of the vapour pressure at different times after the application of the ramp. According to the previously mentioned criterion for the bed lifting, the disturbance may occur at 8.5 ± 0.3 cm from the bottom, about 70 s after the execution of the ramp. The average speed of propagation of the vapour front during this period is found to be 0.22 mm s^{-1}. This front displacement, caused by the fast growth of the initially small boiling zone, can be viewed in Fig. 12.

As the channels permit an easy escape of the vapour towards the liquid pool, the top part of the bed is

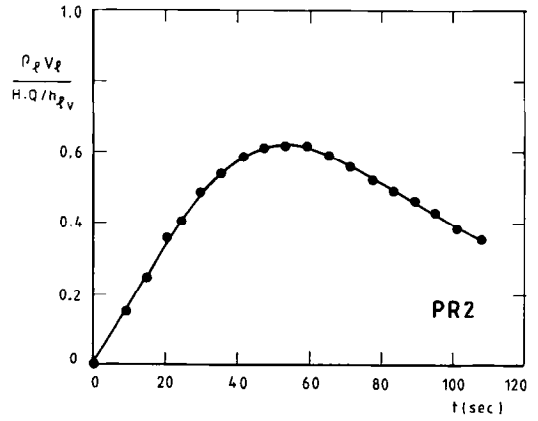

FIG. 10. Computed top liquid flux during PR2.

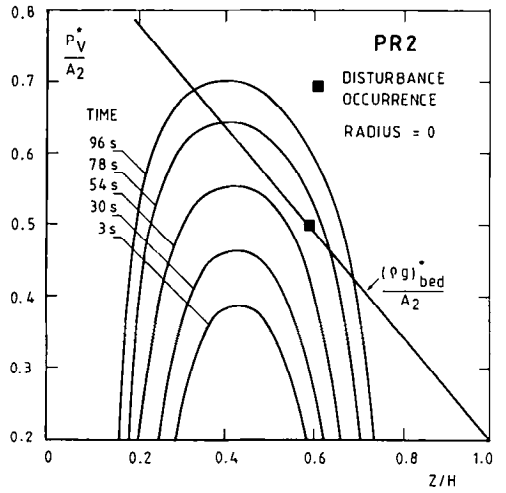

FIG. 11. Computed profiles of vapour pressure during PR2.

almost self-coolable and the coolability of the system is expected to improve. Indeed dryout was detected at a power level of about 1.12 W g^{-1} showing a significant increase in comparison with the value of 0.55 W g^{-1}, typical of packed dryouts under similar conditions [10].

A similar analysis for the first power ramp performed (PR1, Fig. 13) may justify why it did not cause any disturbance. The temperature profiles in Fig. 14 and the Na level in Fig. 15 are only slightly affected. The computed values follow closely the experimental ones except for the rewetting period, where the model exhibits a certain time delay due to the well-known hysteresis presented by the capillary pressure in porous media. Actually if the Leverett function for imbibition is used, the comparison improves substantially (Fig. 15). The requirement described in equation (14) is not satisfied. The reason for this should not only be sought in the weakness of the

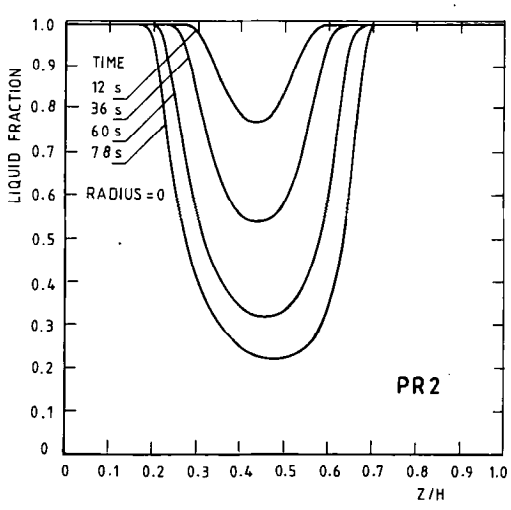

FIG. 12. Computed expansion of the boiling zone during PR2.

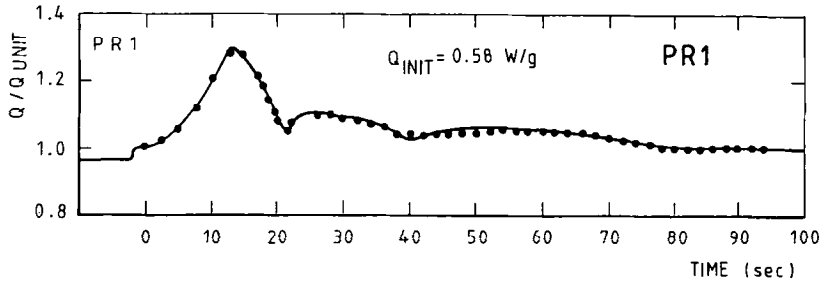

FIG. 13. PIRAMID-1 in-pile experiment: the first power ramp (PR1).

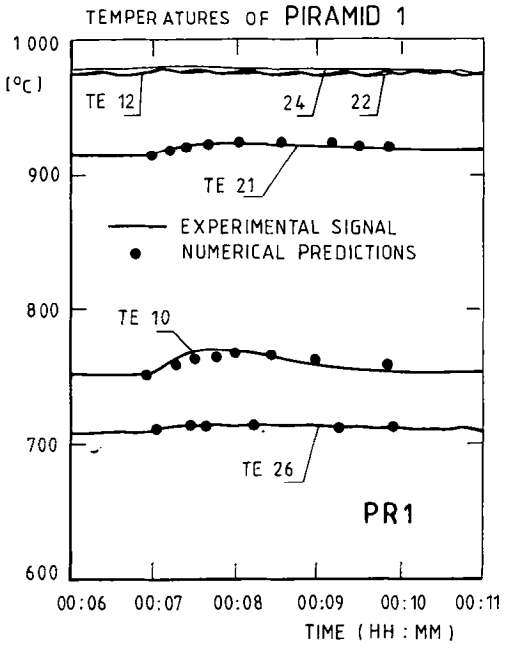

FIG. 14. Experimental and predicted thermocouple histories during PR1.

power ramp itself but also in the initial condition of the bed. A large boiling zone is already present before the ramp giving high initial P_v and the excess of power there is primarily consumed for the decrease of the liquid fraction, rather than for an expansion of the boiling region. Consequently the average propagation speed of the front for this case is predicted as no more than 0.024 mm s^{-1}, one order of magnitude less than the value found for PR2.

D10 test. The effect of the bed initial state and the strength of the power surge emerges again when a simulation of the power ramps performed during the D10 in-pile test is attempted. The bed under consideration consists of UO_2 particles, with an effective diameter of 173 μm, submerged in sodium with an initial height of 0.16 m and a porosity of 38%. In the frame of the 'channel penetration investigations' the power required to induce channelling in the bed was determined by increasing power from about 0.425 W g^{-1} (the incipient packed dryout level) by factors of 1.5, 2.0 and 2.5 with a requenching of the dry zone which had formed following each power step [4]. For the first two ramps a packed bed dry zone was initially present and grew until temperatures reached about

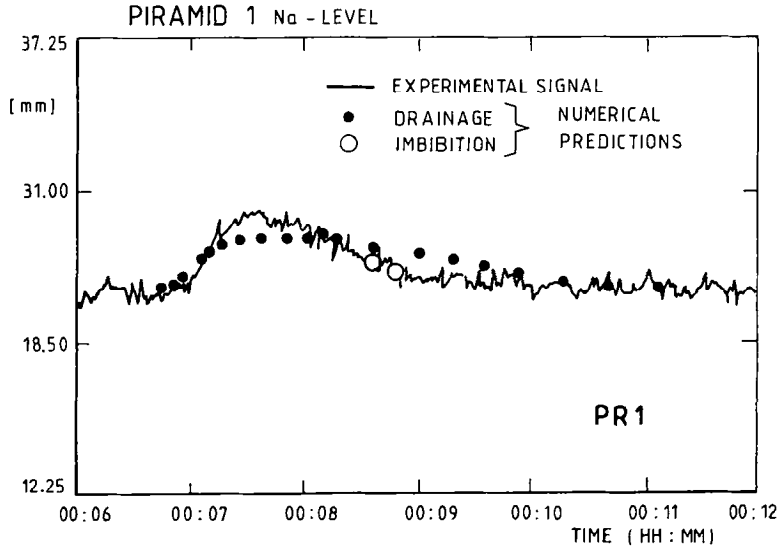

FIG. 15. Experimental and predicted Na level expansion during PR1.

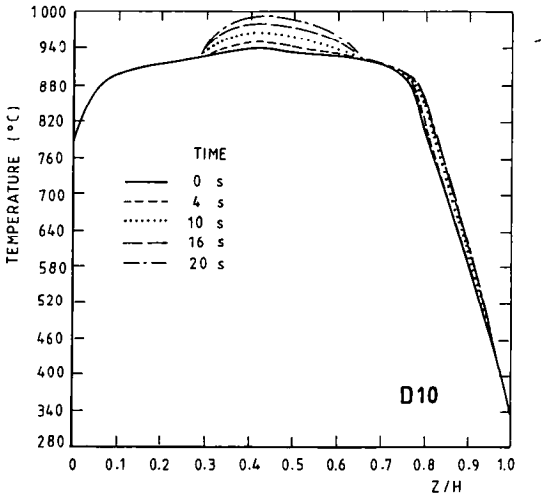

FIG. 16. Temperature evolution during the second D10 power ramp.

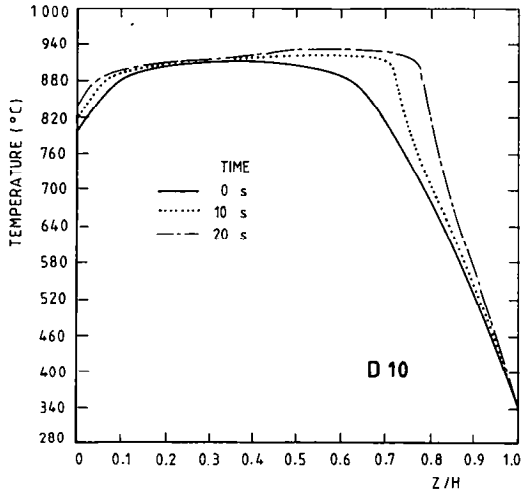

FIG. 17. Boiling zone growth during the third D10 ramp.

1500 K at which time the power was reduced to quench the still expanding dry zone. The calculations for the second of these ramps indicate that with such initial conditions equation (14) cannot be satisfied. Rather, a dry front propagates slowly against a continuously shrinking top boiling zone while the boiling front in itself hardly moves, except for the first few seconds after the ramp. This is clearly shown in Fig. 16 by the evolution of the temperature hump, characteristic of the dry area. The expanding dry region relaxes the vapour pressure field in the bed and acts as a heat sink as it builds up its high temperature gradients. This behaviour does not give rise to disturbances even though the power step is really strong (a factor of 2.0 compared to a factor of 1.7 for the disruptive PR2 in the rather similar PIRAMID-1 bed).

At a power of 1.06 W g^{-1} (the third ramp), a dry zone was not initially present and did not form. About 30 s after the application of the ramp a disturbance was recorded by the thermocouples. In this case of a very pronounced step, Fig. 17 indicates that, according to the model, the initially low situated, already extended, boiling zone grows fast upward for the first 20 s of the transient (at an average speed of 0.96 mm s^{-1}) creating a very steep pressure gradient behind the front. At the same time the maximum vapour velocity reaches the value of 0.5 m s^{-1} which is higher than the 0.47 m s^{-1} predicted, according to ref. [15], for the incipient fluidization of the system. This type of three-phase fluidization is, similar to other systems [16, 17], inherently unstable again resulting in the presence of vapour channels in the disturbed part of the bed.

5. CONCLUSIONS

A study of the transient thermohydraulics of a heat dissipating debris bed submerged in liquid coolant is performed. The physical modelling, based on out-of-pile information, identifies different regimes and heat transfer mechanisms in the bed. Proper mathematical formulation and numerical implementation lead to the development of a computer code for the prediction of the bed behaviour. The applicability of the modelling and the numerical tool is exemplified through the attempted interpretation of typical events of transient nature observed during the first European in-pile test PIRAMID-1 and the D10 experiment at Sandia Laboratories. The effect of steep power ramps is experimentally simulated and the physical mechanism of occurrence of bed disturbances revealed. The observed channel formation is attributed to Taylor instability, an important observation for further modelling developments. Numerical simulations are undertaken using the transient packed bed model, resulting in satisfactory predictions for the boiling zone expansion and the onset of disturbances in the bed. The in-pile data are successfully interpreted on the basis of the computations. The influence of the prevailing bed conditions before the ramp is noticed and investigated leading to useful conclusions for the future in-pile program.

REFERENCES

1. C. Joly and C. Le Rigoleur, General and particular aspects of the particulate bed behaviour in the PAHR situation for liquid metal fast breeder reactors, von Karman Institute LS 1979-04, Fluid dynamics of porous media in energy applications, February (1979).
2. J.-M. Buchlin and T. Van Koninckxloo, O.P.E.R.A. II—a test facility to study the thermohydraulics of liquid saturated self heated porous media, von Karman Institute, TM 41, January (1986).
3. C. Joly, A. Verwimp, J.-M. Buchlin and A. K. Stubos, PIRAMID 1, 2, 3, 4: a complete European PAHR programme in BR2, Mol, Belgium, European Working Group on Irradiation Technology 30th Plenary Meeting, Mol, 28–30 September (1988).
4. G. W. Mitchell, C. A. Ottinger and H. Meister, Cool-

ability of UO_2 with downward heat removal—the D10 experiment, *Proc. 6th Information Exchange Meeting on Debris Coolability*, University of California, Los Angeles, 7–9 November (1984).
5. A. K. Stubos, Boiling and dryout in unconsolidated particle beds, Ph.D. Thesis, Université Libre de Bruxelles, von Karman Institute, April (1990).
6. K. S. Udell, Heat transfer in porous media considering phase change and capillarity—the heat pipe effect, *Int. J. Heat Mass Transfer* **28**, 485 (1985).
7. C. Satik, M. Parlar and Y. C. Yortsos, A study of steady-state steam–water counter-flow in porous media, *Int. J. Heat Mass Transfer* **34**, 1755 (1991).
8. M. Kloker and M. Borsboom, A fully implicit scheme for unsteady flow calculations solved by the approximate factorization technique, von Karman Institute LS 1988-05, Computational fluid dynamics, 7–11 March (1988).
9. M. Borsboom, A. K. Stubos and P.-H. Theunissen, The optimal time step for the implicit approximate factorization scheme—theory and applications, *7th GAMM Conf. Numer. Meth. Fluid Mech.*, Louvain-la-Neuve, 9–11 September (1987).
10. A. K. Stubos, J.-M. Buchlin, C. Pérez Caseiras and C. Joly, Numerical simulation and interpretation of the European in-pile core debris bed experiment, *Expl Heat Transfer* **2**, 257–278 (1989).
11. A. K. Stubos and J.-M. Buchlin, Modeling of vapour channeling behaviour in liquid saturated debris beds, *ASME Trans. J. Heat Transfer* **110**(A), 968 (1988).
12. J.-M. Buchlin, A. K. Stubos, M. Di Francesco and C. Joly, Experimental and physical modeling of two phase heat transfer in fuel debris beds, *J. Heat Technol.* **7**(1), 1–20 (1989).
13. A. K. Stubos, C. Pérez Caseiras, J.-M. Buchlin and C. Joly, Numerical simulation of the transient thermo-hydraulic behaviour of a heat dissipating debris bed, *A.I.Ch.E. Symp. Series* **85**(269), 129–135 (1989).
14. E. D. Chikhliwala, A. B. Huang and Y. C. Yortsos, Numerical study of the linear stability of immiscible displacement in porous media, *Transport in Porous Media* **3**, 257–276 (1988).
15. J. D. Gabor, J. C. Cassulo, D. Fountain and J. D. Bingle, Gas fluidization of solids in a stationary liquid, *A.I.Ch.E. Symp. Series* **80**(241), 95 (1984).
16. D. Green and G. M. Homsy, Instabilities in self-fluidized beds—I, *Int. J. Multiphase Flow* **13**(4), 443 (1987).
17. D. Green and G. M. Homsy, Instabilities in self-fluidized beds—II, *Int. J. Multiphase Flow* **13**(4), 459 (1987).